Direct imaging of rapid tethering of synaptic vesicles accompanying exocytosis at a fast central synapse

Takafumi Miki[a,b,1], Mitsuharu Midorikawa[c], and Takeshi Sakaba[a,1]

[a]Graduate School of Brain Science, Doshisha University, 610-0394 Kyoto, Japan; [b]Organization for Research Initiatives and Development, Doshisha University, 610-0394 Kyoto, Japan; and [c]Division of Neurophysiology, Department of Physiology, School of Medicine, Tokyo Women's Medical University, 162-8666 Tokyo, Japan

Edited by Thomas C. Südhof, Stanford University, Stanford, CA, and approved May 6, 2020 (received for review January 6, 2020)

A high rate of synaptic vesicle (SV) release is required at cerebellar mossy fiber terminals for rapid information processing. As the number of release sites is limited, fast SV reloading is necessary to achieve sustained release. However, rapid reloading has not been observed directly. Here, we visualize SV movements near presynaptic membrane using total internal reflection fluorescence (TIRF) microscopy. Upon stimulation, SVs appeared in the TIRF-field and became tethered to the presynaptic membrane with unexpectedly rapid time course, almost as fast as SVs disappeared due to release. However, such stimulus-induced tethering was abolished by inhibiting exocytosis, suggesting that the tethering is tightly coupled to preceding exocytosis. The newly tethered vesicles became fusion competent not immediately but only 300 ms to 400 ms after tethering. Together with model simulations, we propose that rapid tethering leads to an immediate filling of vacated spaces and release sites within <100 nm of the active zone by SVs, which serve as precursors of readily releasable vesicles, thereby shortening delays during sustained activity.

synapse | presynapse | synaptic vesicle | vesicle recruitment

Synaptic vesicle (SV) fusion occurs repetitively at a release site during presynaptic action potential (AP) firing (1, 2). Once an SV at a release site is released, the next vesicle is reloaded to become fusion competent at the site, through reuse of the fusion site (3–6). The reloading of SVs is crucial for sustained transmission during neuronal activity (7). During reloading, SVs need to 1) be tethered to the active zone (AZ), 2) docked at presynaptic membrane, and 3) have assembled an elaborate release apparatus (primed) to be ready for release. In the tethering step, vesicles are recruited from a recycling/releasable pool containing several hundreds of vesicles near the AZ (8). Then vesicles are attached to the presynaptic membrane, turning into docked vesicles (9). The last priming step is mediated by vesicle–AZ protein complex, which constitutes a release machinery (10–12). Recently, it was proposed that docking and priming are the same process, such that priming molecules dock the vesicles to the membrane and prepare vesicles for release at the same time (13, 14). The rate of vesicle reloading including these two or three steps was estimated by electrophysiological studies together with model simulations (5). Although these studies provide useful mechanistic insights, it has been difficult to differentiate between these steps without direct observation. The mechanisms of docking/priming have been deciphered by in-depth morphological analysis and electrophysiological examinations with knockout (KO) animals (13–16). However, the mechanism of tethering remains largely unknown. In addition, the relative importance of tethering vs. docking/priming remains to be determined.

In the cerebellum, granule cells receive sensory information of different origins at a remarkably high rate through cerebellar mossy fiber (cMF) terminals and convey it to the cerebellar cortex, achieving rapid information processing (17). The firing rate of cMF terminals providing the information to the granule cells increases instantaneously up to 1 kHz in vivo and in vitro (18–20). To achieve synaptic transmission at such a high frequency, SVs at cMF terminals need to be rapidly reloaded at release sites (21, 22). A limited number of readily releasable vesicles and high release probability (Pr) of vesicles (>0.6) at the limited size of AZs demand very high speed of SV reloading during sustained activity, which is also a requirement at other synapses with few AZs (21, 23–27). However, the mechanism of SV reloading remains unclear at cMFs, due to lack of direct observation. In particular, it is unknown how fast each step of docking/priming and tethering occurs during rapid SV reloading. The mobility of vesicles in cMF terminals has been investigated using the photobleaching technique (28), but direct observation of vesicle recruitment to the presynaptic membrane has not been reported.

In this study, we directly examined the kinetics of SV reloading by observing movements of fluorescently labeled vesicles near the presynaptic membrane in acutely dissociated cMF terminals. We use a total internal reflection fluorescence (TIRF) microscopy approach that illuminated labeled vesicles only in the evanescent field (~100 nm; refs. 29–32). By TIRF imaging, we found that resident vesicles rapidly disappeared due to exocytosis, while new vesicles appeared very rapidly in the TIRF field. Based on the experimental results and model simulations, we propose that efficient coupling of tethering, vesicle priming, and exocytosis within the limited space of AZ can maintain kilohertz synaptic transmission.

Significance

At mammalian synapses, synaptic vesicles need to be rapidly reloaded to the limited membrane of transmitter release sites during repetitive firing, but the underlying mechanisms remain unclear. In this study, we directly visualized individual synaptic vesicle dynamics near presynaptic membrane of the cerebellar mossy fiber terminal using total internal reflection fluorescence microscopy. Synaptic vesicles became tethered to the presynaptic membrane with unexpectedly rapid time course, almost as fast as synaptic vesicle release. Such newcomers cannot be fusion competent immediately, and additional priming time of 300 ms to 400 ms was required. We propose a mechanistic model which explains how efficient coupling of tethering, vesicle priming, and exocytosis within the limited space of presynaptic active zone can maintain kilohertz synaptic transmission.

Author contributions: T.M. designed research; T.M. performed research; T.M. analyzed data; T.M., M.M., and T.S. wrote the paper; T.M. and T.S. interpreted data; and M.M. established experimental equipment.

The authors declare no competing interest.

This article is a PNAS Direct Submission.

[1]To whom correspondence may be addressed. Email: tmiki@mail.doshisha.ac.jp or tsakaba@mail.doshisha.ac.jp.

This article contains supporting information online at https://www.pnas.org/lookup/suppl/doi:10.1073/pnas.2000265117/-/DCSupplemental.

First published June 8, 2020.

Results

Rapid Tethering of SVs at Dissociated Cerebellar Mossy Fiber Terminals. To investigate SV movements near presynaptic membrane, we established the method to observe individual SV by TIRF microscopy at dissociated cMF terminals (20, 21). Because the evanescent light only illuminates a thin field in TIRF microscopy, we could only observe those vesicles labeled by the styryl dye *N*-(3-Triethylammoniumpropyl)-4-(4-(Dibutylamino) Styryl) Pyridinium Dibromide (FM 1-43, FM) which were in proximity to the presynaptic membrane (<~100 nm). We sparsely labeled the vesicles by optimizing the period of staining so that we could investigate fusion and movement into and/or out of the TIRF field at the level of single vesicles (29–31). The dissociated cMF terminals from cerebellar slices were identified by their morphology, FM labeling, and electrophysiological properties. Fig. 1*A* shows the characteristic morphology of a dissociated terminal with an uneven surface and filopodia-like structure attached to the coverslip. In addition, a TIRF image where FM-labeled bright spots were observed is shown. Presynaptic features such as APs, Ca^{2+} currents, and capacitance increases were measured by electrophysiological recordings at the cMF terminals (*SI Appendix*, Fig. S1 and Fig. 1*B*). The capacitance jump (ΔC_m) in response to a 0-mV depolarization pulse for 100 ms positively correlated with peak Ca^{2+} current, basal membrane capacitance, and slope of the capacitance increased after the depolarization pulse (mean ± SEM: 56.3 ± 5.6 fF, 174.8 ± 11.3 pA, 1.93 ± 0.11 pF, and 94.6 ± 5.05 fF·s^{-1} for ΔC_m, peak Ca^{2+} current, membrane capacitance, and slope of the capacitance increase, respectively), indicating that larger terminals have more capacity for SV release (Fig. 1*C*). The plots of capacitance jumps for different pulse durations were fitted with a single exponential function having τ_1 of 10.2 ms and a line with a slope of 49.8 fF·s^{-1}, suggesting two components of vesicle release, which may represent release from the readily releasable pool (RRP) and sustained release of newly reloaded SVs during stimulation (*SI Appendix*, Fig. S1*B*).

At identified cMF terminals, we investigated individual SV movements using TIRF microscopy. We observed individual SVs as bright spots, the sizes of which are close to a diffraction limit (σ = 100 nm to ~130 nm; *SI Appendix*, Fig. S1*C*). The labeled subpopulation is thought to be representative, because endocytosed vesicles are reused for release through recycling and releasable pools within several minutes (33), and the time course of capacitance increase matched relatively well with that of fusion events observed by TIRF microscopy (see below). We defined "vanish" and "tethering" types of SV events as previously reported (refs. 30 and 31 and Fig. 1*D*). "Vanish" events are bright spots visible at the onset of recordings and disappearing from the TIRF field. "Tethering" events are the spots appearing and staying thereafter in the TIRF field (Fig. 1*D*). In some cases, the spots appeared and then disappeared during recordings ("tethering–vanish" event; *SI Appendix*, Fig. S2). "Vanish" events include exocytosis and vesicle-undocking from the plasma membrane. In a subset of "vanish" events, we found "diffuse" events during which fluorescence was spreading out from the spot while it was disappearing (*SI Appendix*, Fig. S1*D*; see also *SI Appendix*, Fig. S3), which clearly indicates SV exocytosis (29). "Tethering" events represent SV tethering presumably to the AZs, because hundreds of AZs are densely localized at a single cMF terminal (28, 34).

To examine the effects of stimulation on "vanish" and "tethering" events, we performed whole-cell recording with simultaneous TIRF imaging at dissociated cMF terminals. Applying a 0-mV depolarization pulse for 100 ms induced an increase of membrane capacitance and of the number of "vanish" and "tethering" events (Fig. 1 *E* and *F*). Cumulative plots of the number of events demonstrated that "vanish" and "tethering" events took place upon a depolarization pulse with time constants of τ_1 = 10 ms and τ_2 = 225 ms for "vanish" events, and a time constant of 188 ms for "tethering" events (Fig. 1*F*). The almost simultaneous occurrence of vanish and tethering events is specific for cMF terminals because "tethering" events were not markedly induced during depolarizing pulses at the calyx of Held and at hippocampal mossy fiber terminals (30, 31). Low rates of vanish and tethering events before stimulation were observed at cMF terminals as previously reported at dissociated calyx of Held and hippocampal mossy fiber terminals (30, 31). We should note that basal vanish events most likely reflect untethering because the events were insensitive to tetanus toxin (TeNT), as described below.

To test whether SV tethering takes place during physiological neuronal activity, we performed cell-attached recording to evoke APs at 50 Hz without changing the intracellular environment (Fig. 1*G*). In this experiment, stimulus-induced "tethering" events were observed together with "vanish" events, although the overall time courses were slower than those evoked by a depolarization pulse. Cumulative numbers of events were fitted by single exponential curves with time constants of 755.3 and 1,094 ms for "vanish" and "tethering" events, respectively (Fig. 1*H*). TIRF imaging at high temperature (using a 100-ms pulse protocol) also showed simultaneous occurrence of "tethering" events with "vanish" events (time constants: τ_1 = 10 ms and τ_2 = 490 ms for "vanish" events and 484.8 ms for "tethering" events; *SI Appendix*, Fig. S1*E* and ref. 35). These results suggest that SV tethering occurs simultaneously with SV release or immediately following SV release during neuronal activity.

TeNT Abolished Not Only Stimulus-Induced "Vanish" Events but also "Tethering" Events. It has been reported that SV recruitment depends on presynaptic $[Ca^{2+}]_i$ (36). That raises the question of whether rapid vesicle tethering occurs without vesicle release, when $[Ca^{2+}]_i$ increases at presynaptic terminals by stimulation. To address this, we examined whether stimulus-induced "tethering" events occurred when we applied TeNT, which cleaves VAMP proteins composing soluble N-ethylmaleimide sensitive fusion protein attachment protein receptor (SNARE) complex and blocks exocytosis (37). After establishment of whole-cell mode with a patch pipette filled with an internal solution containing 500 nM TeNT, TeNT gradually blocked capacitance increase without changing Ca^{2+} currents (Fig. 2*A*). We performed TIRF imaging 10 min to 15 min after break-in, and found that the stimulus-induced "vanish" and "tethering" events were abolished, although the basal events still remained (Fig. 2*B*), suggesting that stimulus-dependent "tethering" events could not be induced by the $[Ca^{2+}]_i$ increase alone. Vesicle tethering may be mediated by SNARE-complex formation or may depend on exocytosis (see *Discussion*). The complete blockage of stimulus-induced "vanish" events by TeNT revealed that the stimulus-induced "vanish" events represented SV exocytosis. On the other hand, the unaffected basal events related to "vanish" events suggested that the basal "vanish" events represented Synaptobrevin/VAMP-independent fusion unrelated to glutamate release, or the untethering of SVs. Basal "tethering" events were also insensitive to TeNT and occurred constantly and simultaneously with the basal "vanish" events, suggesting that these vesicles simply enter the TIRF field and then exit it.

TeNT experiments provided further information on "tethering–vanish" events (*SI Appendix*, Fig. S2). As introduced above, "tethering–vanish" events include events of SV tethering/untethering and of SV tethering/release. In the presence of TeNT that blocks exocytosis, only SV tethering/release must have been blocked. When comparing dwell times of the bright spots in presynaptic membrane "tethering–vanish" events between control and TeNT conditions, we found that dwell times were shorter under TeNT conditions, suggesting that the events with

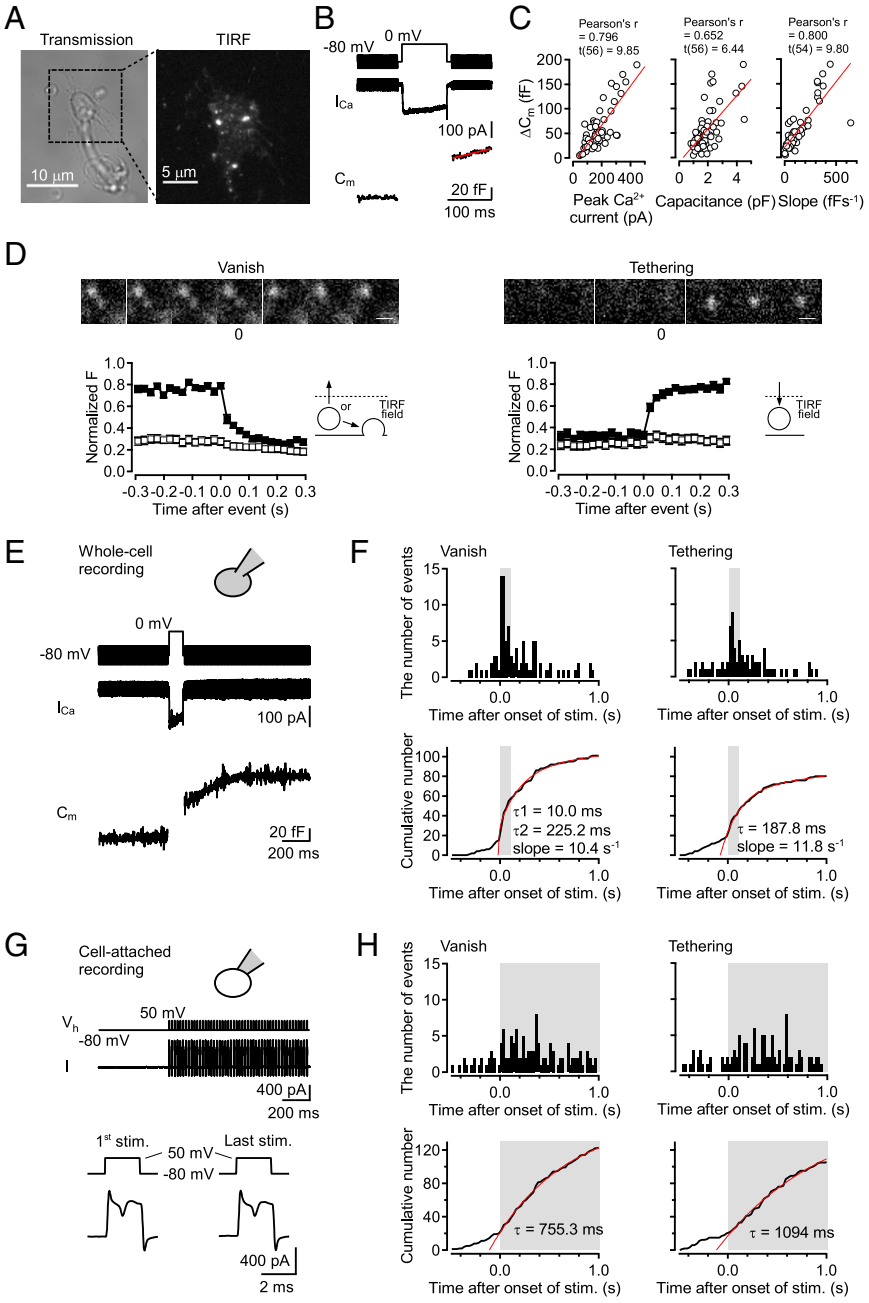

Fig. 1. Rapid vesicle tethering upon a depolarization pulse and APs at dissociated cMF terminals. (*A*) An example of transmitted light image of a dissociated cMF terminal. The expanded image was obtained using TIRF microscopy. SVs were labeled by FM1-43. (*B*) Representative traces of 100-ms depolarization-induced Ca^{2+} current (I_{Ca}) and capacitance jump (C_m). The slope of the capacitance increase after the depolarization pulse was fitted with a line shown in red. (*C*) The amount of capacitance increase by a 0-mV depolarization pulse for 100 ms was plotted against peak Ca^{2+} current, basal membrane capacitance of the recorded terminals ($n = 58$), and the slope of the capacitance increase after the depolarization pulse ($n = 56$). Data from individual terminals were plotted by open circles. These plots were fitted with a line shown in red. (*D*) We observed "vanish" and "tethering" types of vesicle movements in TIRF image. (*Top*) Examples of the two types of events in TIRF image. (*Bottom*) Averages of the normalized fluorescent intensity were plotted against time for 347-nm-diameter circle centered on the spots (filled squares) and the concentric annulus around the circles (outer diameter of 867 nm; open squares). Error bars show SEM ($n =$ 35, and 31 for vanish and tethering, respectively). "Vanish" events correspond to vesicles moving out from the TIRF field or vesicles undergoing exocytosis. "Tethering" events correspond to vesicles recruiting to the TIRF field. (Scale bars, 500 nm.) (*E*) Using whole-cell mode, Ca^{2+} current and capacitance change upon a depolarization pulse were recorded. (*F*) Two types of events were observed by simultaneous TIRF imaging. Peristimulus time histograms for the two types of events and cumulative number of the events from 56 terminals are shown. Fits consist of the sum of a double exponential function and a line for "vanish" events, and the sum of a single exponential function and a line for "tethering" events. According to the result of the different pulse duration experiments (*SI Appendix*, Fig. S1*B*), τ_1 for "vanish" events was fixed at 10 ms. The fit has a ratio of the amount of first to second component of 0.06. The 100-ms depolarization pulse was applied from 0 s to 0.1 s. The depolarizing period is indicated by the gray color (the same for subsequent figures). (*G*) In cell-attached mode, APs were evoked by 2-ms depolarization pulses at 50 Hz for 1 s. (*H*) Peristimulus time histograms and cumulative number of events detected by simultaneous TIRF imaging from 43 terminals. The time of the train is indicated by the gray color. The cumulative numbers of the events were fitted with a single exponential curve (red).

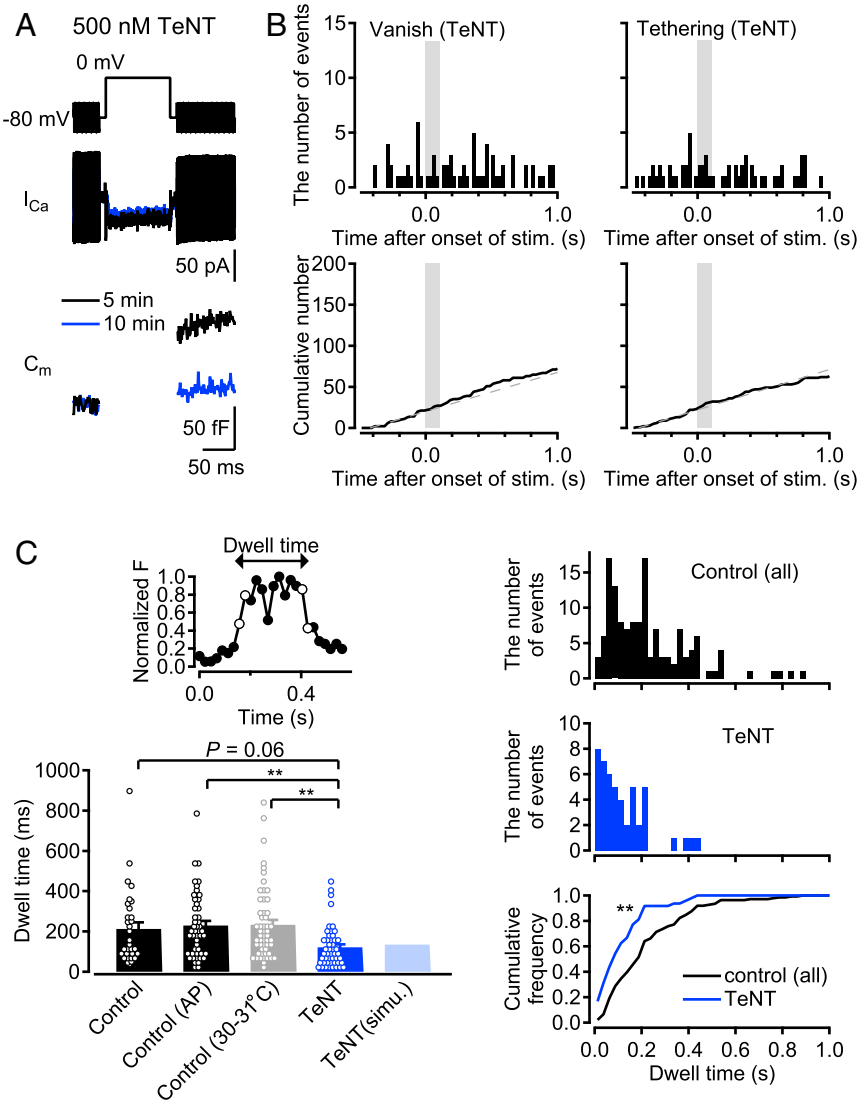

Fig. 2. The effects of TeNT on "tethering" and "vanish" events. (*A*) TeNT (500 nM) was applied by adding to the internal solution for a patch pipette. Example traces were recorded at 5 and 10 min after break-in (black, and blue, respectively). (*B*) (*Top*) Peristimulus time histograms for "vanish" and "tethering" events detected by TIRF imaging at the TeNT-treated terminals ($n = 26$ terminals). A 100-ms depolarization pulse was applied from 0 s to 0.1 s. The stimulation time period is indicated by the gray color. (*Bottom*) The cumulative numbers of each event are shown. Gray dashed lines show fits of the cumulative number of events between −0.5 s and 0 s, representing basal "vanish" and "tethering" events. (*C*) (*Top Left*) An example of the normalized fluorescent intensity for 347-nm-diameter circle centered on the spot in "tethering–vanish" events (filled circles). Open circles show the times of occurrence of the bright spot appearing ("tethering") and disappearing ("vanish"). Dwell time is defined as the time difference between the times of occurrence of "tethering" and "vanish." (*Bottom Left*) Average dwell time of "tethering–vanish" events in various experimental conditions and a simulation for the TeNT experiments ($n = 32$, 49, 55, and 48 for control, AP, high-temperature, and TeNT experiments, respectively). Individual data are shown by open circles. Error bars show SEM. $^{**}P < 0.01$, one-way ANOVA followed by Tukey's test. (*Top Right*) Distributions of the dwell times of "tethering–vanish" events in all control, AP, and high-temperature experiments, and (*Middle Right*) in the TeNT experiment. (*Bottom Right*) Corresponding cumulative distributions of dwell time for control (black) and TeNT (blue). $^{**}P < 0.01$, Kolmogorov–Smirnov test.

shorter dwell times reflect rapid vesicle tethering/untethering, or so-called "bouncing" (mean ± SEM: 212.1 ± 32.3 ms, and 121.4 ± 14.8 ms for control and TeNT, respectively; Fig. 2*C*). In AP experiments using cell-attached modes as well as pulse modes at high temperature, the average values of the dwell time for "tethering–vanish" events were similar to those in control (mean ± SEM: 229.7 ± 22.9 ms, and 233 ± 24.4 ms for AP and high-temperature experiments, respectively). The dwell time histograms demonstrated that events with longer dwell time (>200 ms) tended to be abolished in the presence of TeNT (Fig. 2*C* and *SI Appendix*, Fig. S2*B*). In fact, the fraction of long dwell time events (>200 ms) was 18.7% for TeNT, in contrast to 43.7%, 53.1%, and 47.3% for control, AP, and high temperature conditions, respectively. These results suggested that events with short dwell time (<200 ms) tended to represent SV bouncing unrelated to exocytosis, while longer dwell time events (>200 ms) presumably included SV tethering/release (see *Discussion*).

The Fate of Newly Tethered SVs. We set out to answer how quickly newly tethered vesicles could be released. The dwell time of "tethering–vanish" events in the TeNT experiments (Fig. 2) suggested that the tethered vesicles could not be released immediately (at least > 200 ms). However, in the experiments presented so far, we only applied a single depolarizing pulse, so

that the tethered vesicles may not be exposed to sufficiently high $[Ca^{2+}]_i$ necessary for as high Pr as observed in stimulus-evoked "vanish" events. Rather, they may be only exposed to residual $[Ca^{2+}]_i$ similar to sustained asynchronous release. To test whether the newly tethered SVs can be released immediately, we performed double-pulse experiments in which 30-ms depolarization pulses were applied with an interval of 100 ms. As shown in Fig. 3 *A* and *B*, the first 30-ms depolarization pulse (sufficient to deplete the RRP) did not produce a steep slope of capacitance increase after the pulse, whereas the second pulse did (slope: 25.1 ± 11.0 fF·s^{-1} and 95.4 ± 12.7 fF·s^{-1} for the first and the second pulses, respectively), indicating that sustained release was not strongly induced following the first pulse. Thus, in this experiment with TIRF imaging, we could examine whether the newly recruited vesicles at the first pulse could be released as the fast component of release at the second pulse, since a majority of the vesicles newly recruited at the first pulse were not likely released as sustained release between the first and second pulses. Analysis of TIRF imaging demonstrated that stimulus-induced "vanish" events following the first and the second pulses occurred with time constants of 10.0 and 74.0 ms for the first response, and 68.2 ms for the second response, while the "tethering" events were induced by the first and second pulses with time constants of 99.4 and 107.2 ms, respectively (Fig. 3*C*). A total of 74 vesicles appeared as newly tethered vesicles between the first and second pulses. Out of these, 30 vesicles disappeared within 1.5 s after the second pulse, while the rest remained thereafter. Peristimulus time histograms of the 30 events which disappeared after the second pulse showed that such events occurred quite randomly (Fig. 3*D*). Only one vanish event was observed during the second pulse, suggesting that a majority of the fast component of release during the second pulse was mediated by the vesicles tethered before the first stimulation, but not by the newcomers. The average dwell time of the 30 events was 439.6 ± 55.5 ms, and 70% of the events had >200-ms dwell time. We measured the time course by fitting the cumulative number of the 30 vanish events with a single exponential function, suggesting that the newcomers disappeared with a time constant of 460.5 ms. The average dwell time could be longer, since the 44 events still remain unfused after the recording period. Newcomers between the pulses may mix with those after the second pulse and residents (vesicles tethered before stimulation), so that some newcomers remain unfused after Ca^{2+} returns to basal level and fusion stops. In 7 out of the 30 vanish events, we could detect fluorescent diffusion representing vesicle fusion (Fig. 3*E* and *SI Appendix*, Fig. S3). The

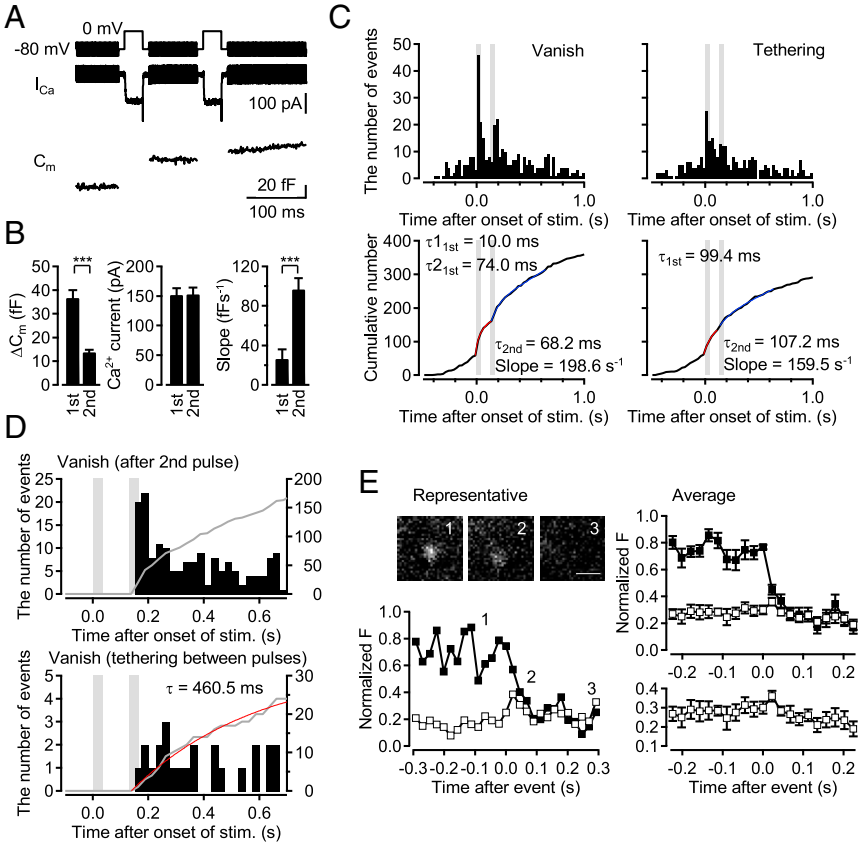

Fig. 3. Newly tethered events contribute to the sustained release at cMF terminals. (*A*) Representative traces for Ca^{2+} current and capacitance in double pulse experiments. Two 0-mV depolarization pulses for 30 ms were applied with an interstimulus interval of 100 ms. (*B*) Ca^{2+} currents and capacitance jumps by the first and the second depolarization pulses, and the slope of the capacitance increase after the pulses were measured (n = 32; mean ± SEM). ***P < 0.001, Student's t test. (*C*) (*Top*) Peristimulus time histograms for "vanish" and "tethering" events observed by TIRF imaging from 80 terminals. The stimulation periods of the pulses are indicated by gray. (*Bottom*) Cumulative numbers of events for the first response were fitted with a single exponential curve (red). Cumulative numbers for the second response were fitted with an exponential curve plus a line (blue). (*D*) Comparison of the time course of fluorescent spots disappearing between total (*Top*) "vanish" events after the second pulse and (*Bottom*) "tethering–vanish" events. In "tethering–vanish" events, the events visibly appearing between 0 ms and 130 ms were analyzed. The cumulative number of vanish events that tether between pulses was fitted with a single exponential curve (red). (*E*) (*Left*) Representative and (*Right*) averaged (n = 7) time courses of the fluorescent intensity within a center (347 nm diameter; filled squares) and concentric annulus (347 nm inner and 867 nm outer diameter; open squares) for "diffuse" events that are tethered between pulses. Average images are taken at the times indicated by numbers. Error bars show SEM. (Scale bar, 500 nm.)

average dwell time of the "tethering–fusion" events was 577.7 ± 121.4 ms, and all events had >200-ms dwell time. The results suggest that newly tethered vesicles were not release competent, but could only be released at least hundreds of milliseconds afterward.

Model Simulation Reveals That Stimulus-Induced Tethering Together with Priming Produces Sustained Release. Based on the double-pulse experiments, we hypothesized that newly tethered vesicles that underwent a subsequent docking/priming step for hundreds of milliseconds could contribute to the release events. To test this hypothesis, we performed model simulations using the values that were obtained experimentally. We assumed two pools, the RRP and the pool for prereleasable vesicles within the TIRF field (TIRF-PRP), and implemented a docking/priming step between the two pools (Fig. 4*A*). In this model, the observed "vanish" events correspond to the release of the readily releasable vesicles, as well as vesicle untethering from the TIRF-PRP, followed by movement out of the TIRF field. "Tethering" events, on the other hand, correspond to vesicle tethering to the TIRF-PRP. In the TeNT experiments, when exocytosis was blocked, only vesicle movements between the inside and outside of the TIRF field established an equilibrium state of the pools (yellow and blue arrows in Fig. 4*A*). The simulation well explained "vanish," "tethering" events, and dwell times of "tethering–vanish" events in TeNT experiments by setting a (basal) tethering rate constant of 6 s^{-1} (Figs. 2*C* and 4*B*). In the simulation for control conditions, we set the time course of tethering events as observed in TIRF imaging. The best fit of the time course of capacitance change (both during and after the pulse) and of "vanish" events was provided by choosing a rate constant of 3 s^{-1} for SV priming to the RRP, and a pool size ratio of RRP/TIRF-PRP = 3 at rest (see *Methods* and Fig. 4*C*). The rate constant for SV priming is thought to be reasonable, because the double-pulse experiments demonstrated that SV priming and subsequent release took ∼400 ms. When eliminating the stimulus-dependent tethering without changing any other parameter (see *Methods*), the slope of the release after a stimulation was decreased (Fig. 4*C*, light colors), indicating that newly tethered vesicles contribute to the sustained release.

In addition, the model simulation provided some insights into SV dynamics within the TIRF field and its relation to exocytosis. The diagrams in Fig. 4*D* show changes in the postulated space

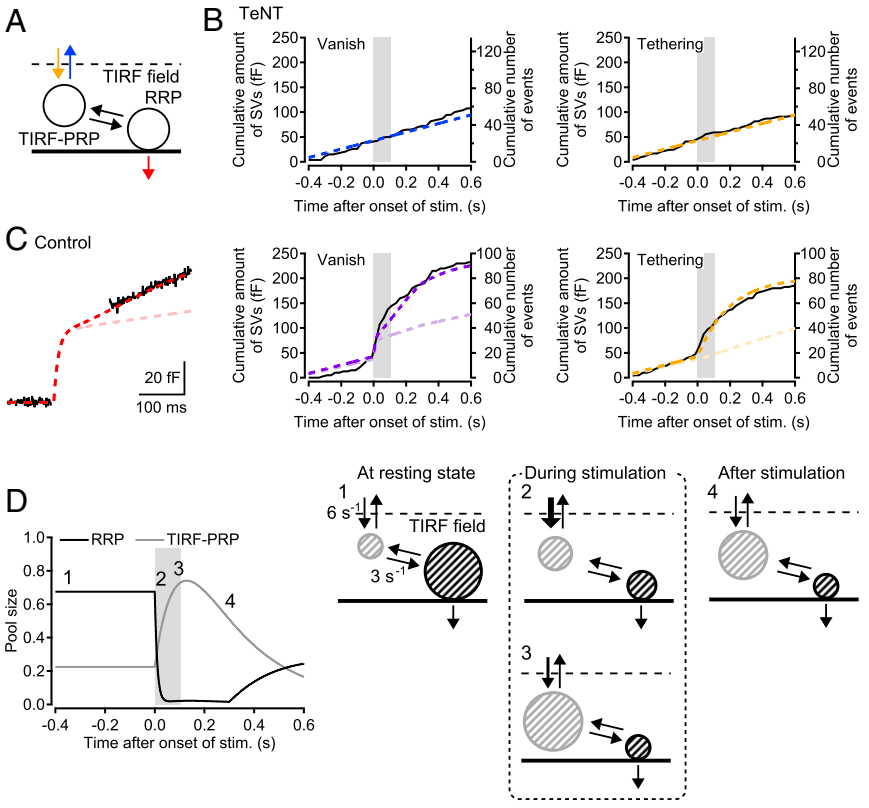

Fig. 4. Model simulation reveals the SV pool dynamics within the TIRF field. (*A*) A sequential two-pool model for SV movement within TIRF field. One pool (TIRF-PRP) is for SVs tethered from outside of the TIRF field, and the other pool (RRP) is for readily releasable vesicles. (*B*) Monte Carlo simulation for the dwell time of the "tethering–vanish" events in the TeNT experiments provide the rate constant of 6 s^{-1} for SV recruitment to the TIRF field (yellow arrow). Since TeNT blocked exocytosis, the vanish and tethering events in the TeNT experiments correspond to SV movements between the outside and inside of the TIRF field to maintain the equilibrium of the occupancy of the pool for tethered SVs. The dashed lines show the corresponding results of the model simulation. (*C*) In the control condition, stimulus-induced tethering events are forced to take place with a time constant of 200 ms in the model to follow the experimental data. Readily releasable vesicles are released with a time constant of 10 ms during stimulation (*SI Appendix*, Fig. S1). The sustained release continues for 300 ms, as we observed in the capacitance increase after stimulation. The best fit of the capacitance increase with the model determines a rate constant of 3 s^{-1} for priming to the RRP (dashed curve in red). The time course of the vanish events representing the sum of release and untethering events is well reproduced by the model (dashed curve in purple). To see changes of the sustained release, the stimulus induced tethering events are abolished in the model (dashed curves in light colors). (*D*) The probabilities of occupancies for the two pools in the TIRF field and schematics of the various phases of the pools (for the data shown in *C*). In the resting state, a space 3 times larger is occupied by the RRP. Once release starts, the space for the RRP immediately becomes close to 0 (see a schema numbered 2). The TIRF-PRP is then overfilled and occupies up to 70 to 80% of the space by rapid tethering (see a schema numbered 3). The newly tethering SVs undergo a SV docking/priming step for 300 ms, in order to be readily releasable for the following sustained release. The stimulation time period is indicated by the gray color in *B*–*D*.

occupancy of the RRP and the TIRF-PRP within the TIRF field. At rest, the RRP occupies 67.5% of the space for vesicle pools near the AZs, while the TIRF-PRP occupies 22.5% of the space, assuming that, at rest, 90% was occupied by RRP and TIRF-PRP. During exocytosis, the RRP was consumed with a time constant of 10 ms (*SI Appendix*, Fig. S1), whereas the TIRF-PRP was overfilled from a low basal level up to 75% of the total size due to rapid, stimulus-induced tethering: The TIRF-PRP can occupy the space vacated by consumption of the RRP. Subsequently, SVs in the TIRF-PRP are converted into readily releasable vesicles through a docking/priming step with a time constant of 333 ms. Finally, these SVs contributed to sustained release. The characteristic feature of the model is that two different pools compete for the space and release sites within the TIRF field (Fig. 4*D*), which can explain the tight coupling between exocytosis and tethering seen at this synapse.

Rapid tethering is beneficial for vesicles to accelerate subsequent vesicle priming, which has to precede exocytosis (38). Such rapid tethering (time constant: 200 ms) is not necessary if the priming process itself is very rapid. We could show this by another type of simulation which assumed tethering with a slow time constant of 700 ms, followed by an instantaneous priming process. This scenario was also able to achieve the high rates of the sustained release (*SI Appendix*, Fig. S4). However, given our finding that priming is slow, the rapid tethering combined with stimulus-induced overfilling of the TIRF-PRP plays a crucial role in supporting synaptic signaling during high-frequency activity. This conclusion may extend to a variety of other synapse types with one or two AZs (see *Discussion*).

Discussion

In this study, we focused on the vesicle reloading to release sites at the cMF terminals using TIRF microscopy. Fast synaptic reloading has been measured at these synapses using electrophysiology, but the underlying mechanisms have not been examined directly. Direct, real-time visualization of single SVs immediately before, during, and after exocytosis has allowed us to gain exciting insights into why these synapses can transmit reliably in the kilohertz range. Unexpectedly, we found rapid vesicle tethering into the TIRF field at cMF terminals during stimulation (time constant: 100 ms to 200 ms; Fig. 1). Most of the vesicles consumed by stimulus-evoked exocytosis were immediately replenished by newly tethered vesicles. Rapid tethering was sensitive to TeNT, suggesting SNARE dependence (Figs. 2 and 3). The double-pulse experiments suggested that newly tethered vesicles in the TIRF field could not reach fusion competence immediately (Fig. 3). Model simulations suggested that it took newly tethered vesicles several hundred milliseconds to be converted into the readily releasable states. The modeling also suggested that the limited space in the AZ is efficiently used by an expanded TIRF-PRP occupying space previously vacated by RRP vesicles (Fig. 4), thus achieving repetitive vesicular releases at high frequencies.

The Two Pools Share the Space within the TIRF Field and Mediate Rapid SV Reloading. In TIRF imaging with electrophysiological stimulation, we found that vesicle release and tethering took place almost simultaneously during a long depolarization pulse (Fig. 1). The speed was much faster than at other synapses measured so far, such as ribbon synapses of retinal bipolar cells (ref. 29; but see ref. 39) as well as conventional synapses of the calyx of Held and hippocampal mossy fibers (30, 31). At these conventional synapses, tethering occurred slowly after depletion of the RRP, implying that tethering and exocytosis are not tightly coupled like at cMF terminals. It is possible that large terminals with multiple release sites do not require fast tethering, whereas cMF synapses, which have a small number of release sites per synaptic connection, require faster tethering. Both tethering and fusion events were blocked by TeNT (Fig. 2). The results can be explained by two possibilities: One is that the tethering events require intact synaptobrevin (SNARE complex) for stabilization, while the alternative is that the events depend on the space at the release sites, which can become available only by exocytosis. Cryoelectron tomography demonstrated that the TeNT treatment did not change the number of tethering vesicles in the proximal to the AZ (40). Likewise, synapses lacking synaptobrevin-2 also showed no changes in the number of SVs within 100 nm of the AZ (13). Considering these electron microscopy studies, it is unlikely that SNARE complexes directly regulate vesicle tethering. Studies of synaptotagmin-1 mutants and KOs demonstrated that vesicle docking/membrane translocation, which precedes formation of the SNARE complex, was defective in these mutant and KO cells (14, 41). Recent reports suggest that synaptotagmin-7 mediates facilitation, asynchronous release, and sustained release, likely due to its function in vesicle replenishment (42–46). Synaptotagmin-7 is abundantly expressed at hippocampal mossy fiber terminals, which do not have such a rapid tethering, but is not expressed at cMF terminals (31, 43, 46). Therefore, synaptotagmin-1 and/or synaptotagmin-7 might regulate the rate of the vesicle tethering.

Immediate vesicle tethering at cMF terminals suggested a tight coupling between tethering and exocytosis, suggesting that newly tethered unprimed vesicles and primed vesicles share the space within a limited region around the AZ. Model simulations also indicated that rapid tethering leads to an exchange of the RRP with the TIRF-PRP within the 100 ms following exocytosis (Fig. 4). Note that the RRP may further be split into two release components (high-Pr and low-Pr vesicles; refs. 20 and 47), although we did not separate the components in this study. Under physiological conditions, the tethering time constant was much slower (1 s) than the time constant of the tethering upon a strong depolarization pulse (Fig. 1). According to the model simulation, that is because the space for newcomer opens slowly under the condition, due to the slow release time constant (760 ms). Because of *z*-axis resolution, TIRF-PRP may comprise a fraction of the PRP, which is extended beyond the depth of 100 nm (but see morphological features of a tethered vesicle pool below). At presynaptic boutons in the central nervous system, there are several hundred SVs at a density of ∼1,000 μm^{-3}, or even more in the proximity of AZ (8, 28, 48). Docked/primed vesicles are directly attached to or within 5 nm of the plasma membrane and comprise the RRP, while tethered vesicles are attached via filament-like structure within ∼45 nm of the AZ (13, 40, 49). Therefore, the vesicles observed within the TIRF field (<100 nm) mainly correspond to the docked/primed and tethered vesicles, given the vesicle diameter of 40 nm to 50 nm. The morphological observations also indicate that docked vesicles and tethered vesicles fill the space near AZs, and are so dense that other vesicles cannot easily access the presynaptic membrane because of the steric hindrance of vesicles (50). Consistent with this hypothesis of limited space for vesicle priming, it has recently been reported that the number of undocked vesicles in >10 nm of AZ was increased when the number of docked vesicles was reduced upon AP stimulation (51). Furthermore, after genetic KO of priming molecules Munc13-1 and Munc13-2 or CAPS, the synapses showed redistribution of SVs without a large change in the SV number within 100 nm of the AZ (13, 52). The number of vesicles closer than 10 nm to the AZ was reduced, whereas the SV number at 20- to 40-nm distance to the AZ was increased in the KO synapses, suggesting priming does not change the total number of vesicles that are <50 nm from the AZ.

SV Priming at cMF Terminals. "Tethering–vanish" events represent both tethering–untethering events and tethering–release events. The histogram of the dwell time of "tethering–vanish" events in control stimulation showed one peak at 50 ms to 75 ms and a

long tail or second peak at 200 ms to 225 ms, indicating two discrete types of events (Fig. 2 and *SI Appendix*, Fig. S2*B*). We believe most transiently tethered events with dwell time of <200 ms are not related to the fusion of newcomers, but rather reflect bouncing. This is because fast events were not blocked by TeNT, which blocks all of the fusion events in both TIRF microscopy and capacitance measurements. Because the dwell time of bouncing events in TeNT experiments is 120 ms on average, dwell time of the tethering–release events is >200 ms, considering the mean time of the TeNT-sensitive "slow" events. In other words, we have directly observed the fate of SVs from arrival to fusion, in mammalian central nervous system, and measured a so-called "priming time" of 300 ms to 400 ms. Model simulations provided a rate of vesicle docking/priming of 3 s^{-1}, which is consistent with the above estimate. The value is comparable to ribbon synapses of goldfish retinal bipolar cells (Fig. 4 and ref. 29). Midorikawa and Sakaba (30) have speculated a similar value at the calyx of Held from TIRF measurements combined with Ca^{2+} uncaging, but they did not observe the fate of vesicles from arrival to fusion directly. Because they have not seen tethering–vanish events, it is likely that the PRP is larger than the RRP at the calyx of Held synapse. Recovery of synaptic responses after train stimulation is slow, with a time constant of several seconds (ref. 47; see also refs. 53 and 54). The slow recovery suggests the presence of an activity-driven process in high-frequency situations, or rather reflects "superpriming" of SVs (55).

Vesicle priming most likely involves a common molecular mechanism involving RIM, Munc13, Munc18, SNAREs, CAPSs, and Syt-1 (10, 11, 13, 14, 56–58). It has been recently hypothesized that the transition between loosely and tightly docked/primed states of vesicles in the RRP is dynamic, and occurs within 10 ms to 50 ms (14, 55, 58). Morphological correlates of loosely and tightly docked/primed vesicles are the vesicles attached to plasma membrane and the vesicles located only 5 nm to 10 nm away from plasma membrane, respectively (14, 51, 52). Loosely and tightly docked vesicles correspond to so-called primed and superprimed vesicles (55), respectively. Miki et al. (27, 59) also reported a similar rapid transition of vesicles between the docking sites and replacement sites (a few milliseconds). Such transitions cannot be resolved here by TIRF imaging, and the priming time in this study reflects the entire process from tethering through priming to fusion. In the present study, we estimated the rate of SV priming by measuring the tethering–vanish events after previous release, since the RRP including docked/primed vesicles was immediately depleted upon depolarization pulses or high-frequency stimulation. Therefore, it could be that our priming has to do with site clearance for reuse of release sites (3, 36, 60). Thus we might have overestimated the priming time for an empty release site which has no experience of vesicle fusion.

In the present study, we observed vesicle movements between outside and inside of the TIRF field (<100 nm). Direct imaging allowed us to demonstrate rapid tethering, which had not been directly observed before. While priming, the buildup of the release machinery, requires hundreds of milliseconds, rapid tethering together with dynamic regulation of the TIRF-PRP and RRP enables efficient vesicle reloading and allows rapid information processing in the cerebellum. The cMF synapses have a small number of AZs per synaptic connection, and this is rather similar to cortical synapses (61), resulting in very high demand for a given AZ. Thus, we think that the direct measurement of priming time and mechanistic insights on vesicle tethering at cMF synapses will have general implication.

Methods

Experimental Animals. Male and female Wister rats (postnatal days 21 to 36) were used in accordance with the guidelines of the Physiological Society of Japan. All procedures and animal care were conducted in accordance with the guidelines of the Physiological Society of Japan, and were approved by Doshisha University committee for Regulation on the Conduct of Animal Experiments and Related Activities. All efforts were taken to minimize the number of animals.

Experimental Procedure. Sagittal slices (300 μm thick) were prepared from the cerebellar vermis of male and female Wister rats (postnatal days 21 to 36), following the animal care guideline of the Physiological Society of Japan. The slices were obtained using a Leica VT1200S slicer (Leica Microsystems) in ice-cold slice medium containing (in millimolar) 87 NaCl, 75 sucrose, 25 $NaHCO_3$, 1.25 NaH_2PO_4, 2.5 KCl, 10 glucose, 0.5 $CaCl_2$, and 7 $MgCl_2$. Slices were then incubated at 37 °C for 1 h in a slice medium equilibrated with 95% O_2 and 5% CO_2.

For FM loading, after incubation, slices were set on a glass-bottomed dish (D111300, Matsunami Glass) in the FM loading solution containing (in millimolar) 125 NaCl, 2.5 KCl, 25 $NaHCO_3$, 1.25 NaH_2PO_4, 0.4 ascorbic acid, 3 myoinositol, 2 Na-pyruvate, 25 glucose, 2 $CaCl_2$, 1 $MgCl_2$, and 0.015 FM1-43. Under an upright microscope, a bipolar electrode was positioned on vermal lobules VII and VIII for extracellular stimulation at 2 Hz for 2 min, for a total four times, with changing of the electrode position along the lobules. These were then washed with an artificial cerebrospinal fluid (ACSF) solution containing (in millimolar) 125 NaCl, 2.5 KCl, 25 $NaHCO_3$, 1.25 NaH_2PO_4, 0.4 ascorbic acid, 3 myoinositol, 2 Na-pyruvate, 25 glucose, 2 $CaCl_2$, 1 $MgCl_2$, and 0.001 TTX. After dissecting unnecessary regions, the slices were digested in cysteine (5 mM)-activated papain (5 mg/mL) added to 0.5 Ca ACSF solution containing (in millimolar) 125 NaCl, 2.5 KCl, 25 $NaHCO_3$, 1.25 NaH_2PO_4, 0.4 ascorbic acid, 3 myoinositol, 2 Na-pyruvate, 25 glucose, 0.5 $CaCl_2$, 7 $MgCl_2$, and 0.001 TTX, for 13 min at 37 °C. After washing with a 0.5 Ca ACSF solution with 0.01 mg/mL bovine serum albumin, the slices were mechanically triturated with a fire-polished Pasteur pipette (open diameter of 1 mm) in the ACSF solution. The cell suspension was plated on a glass-bottomed dish coated with concanabalin A. The recording solution containing (in millimolar) 125 NaCl, 2.5 KCl, 25 Hepes, 1.25 NaH_2PO_4, 0.4 ascorbic acid, 3 myoinositol, 2 Na-pyruvate, 25 glucose, 2 $CaCl_2$, 1 $MgCl_2$, and 0.001 TTX (pH 7.4) was added on the glass-bottomed dish 15 min to 25 min after plating. The solution was not perfused or bubbled during the recording, because solution exchange and bubbling could result in movements which distort TIRF imaging. Dissociated cMF terminals were identified based on 1) their characteristic morphology (uneven surface with filopodia-like structures, attached on a coverslip), 2) FM labeling, and 3) inward calcium currents and capacitance jumps in response to depolarization pulses in whole-cell recording, or an AP in response to a depolarization pulse in cell-attached recording (Fig. 1).

Electrophysiological Recording. Dissociated cMF terminals were recorded in whole-cell mode, current clamp mode, or cell-attached mode. In whole-cell mode, the cMF terminals were voltage-clamped at −60 mV using EPC10/2 amplifier (HEKA), controlled by PatchMaster software (HEKA). The patch pipettes were filled with the internal solution containing (in millimolar) 140 Cs-gluconate, 20 TEA-Cl, 10 Hepes, 5 Na_2-phosphocreatine, 4 Mg adenosine triphosphate (MgATP), 0.5 Na guanosine triphosphate (NaGTP), and 0.5 ethylene glycol tetraacetic acid (EGTA, pH 7.3). During recording, the holding potential was set to −80 mV. Membrane capacitance measurements were performed using an EPC10/2 amplifier in the sine + DC configuration (62). A sine wave (30 mV in amplitude, 1,000 Hz in frequency) was superimposed on a holding potential of −80 mV. The pipettes (Harvard, GC-150F-10) had resistance of 13 MΩ to 20 MΩ, and the series resistance was 25 MΩ to 60 MΩ. We stopped recording when the leak currents exceeded 50 pA at the resting potential, or the extent of peak Ca^{2+} current run-down exceeded 50%. Liquid junction potential was not corrected. In current clamp mode, the patch pipettes were filled with the solution containing (in millimolar) 140 K-gluconate, 20 KCl, 10 Hepes, 5 Na_2-phosphocreatine, 5 MgATP, 0.5 NaGTP, and 0.5 EGTA (pH 7.3). The recording solution without TTX was used as an extracellular solution. In cell-attached mode, the patch pipettes were filled with a solution containing (in millimolar) 155 NaCl, 2.5 KCl, 1.25 NaH_2PO_4, 25 glucose, and 3 $MgCl_2$ (pH 7.4). The extracellular solution contained (in millimolar) 125 NaCl, 2.5 KCl, 25 Hepes, 1.25 NaH_2PO_4, 0.4 ascorbic acid, 3 myoinositol, 2 Na-pyruvate, 25 glucose, 1.5 $CaCl_2$, and 6 $MgCl_2$ (pH 7.4). Data were analyzed offline with IgorPro software (Wavemetrics).

TIRF Imaging. Terminals were illuminated by TIRF on the stage of an inverted microscope (ECLIPSE Ti, Nikon) equipped with a 100× oil immersion objective (NA1.49, Nikon). In our recording conditions, the decay constant of the evanescent field was −100 nm (30). A 488-nm laser (OBIS 488-20 LS, Coherent)

was used for FM1-43 excitation, and a 520 long pass filter was used as an emission filter. Images were acquired every 20 ms using a scientific CMOS camera (Zyla, Andor) controlled by SOLIS software (Andor). Image magnification was 150×, and provided 43.3 nm per pixel resolutions on the camera chip. Movies were acquired every 2 min. Voltage pulse and image capture were synchronized by a transistor–transistor logic pulse. Image analysis was performed using ImageJ/Fiji, and Igor software.

Analysis. Image analysis was performed using a combination of Igor and ImageJ/Fiji. Fluorescent spots were rejected if they were unlikely to represent single SVs, that is, if they were blurry, too bright, oblong, or too large to be diffraction limited. After selection, the remaining spots were Gaussian fitted to confirm that they were diffraction limited. To measure the fluorescence time course, the fluorescence of single vesicles was measured within a 344-nm circle centered on the vesicle. For Gaussian fitting of the vesicles, a handmade program on the ImageJ/Fiji was applied. All values were given as means ± SEM. Statistical significance was determined using the Student's *t* test.

The classification of SV events was performed as previously described (30). In brief, "vanish" events were defined as spots that showed sudden diminishing of the fluorescent spots. "Tethering" events were defined as spots that suddenly emerged in the middle of the recordings.

Model Simulation. To examine the effect of the rapid tethering on release in control and to estimate the rate of vesicle priming in the TIRF fields, we established a two-pool model where there are pools for newly tethered, unprimed vesicles and readily releasable vesicles. Although we also tested a one-pool model, it could not explain our data well. The time course of either release or tethering could not be matched by a one-pool model (*SI Appendix*, Fig. S4). For *SI Appendix*, Fig. S4, the number of released vesicles ($N_{release}$) and vesicles in the pool (N_{RRP}) are defined by the following differential equations:

$$\frac{d}{dt}N_{release}(t) = k_{rel}(t)N_{RRP}(t)$$

$$\frac{d}{dt}N_{RRP}(t) = k_{+0}\left(1 - P_{occ,RRP}(t)\right) - k_{-0}N_{RRP}(t) - k_{rel}(t)N_{RRP}(t),$$

where k_{rel} is a release rate constant, k_{+0} is a recruitment rate constant, k_{-0} is a back-rate constant, and $P_{occ,RRP}$ is a probability of occupancy for the RRP. Vesicle release occurs only from 0 s to 0.3 s ($k_{rel}(t) = 100\ s^{-1}$, $0 \le t \le 0.3$; $k_{rel}(t) = 0$, $t < 0$ and $t > 0.3$). The initial occupancy is set to 0.9 ($P_{occ,RRP}(0) = 0.9$). The best fit of the time courses of release and "vanish" events provides k_{+0} of 12 s^{-1} ($k_{-0} = k_{+0}\ (1 - P_{occ,RRP}(0))/N_{RRP}(0)$).

In the two-pool model (Fig. 4), we assumed two pools, the RRP and the TIRF-PRP, both of which have a probability of occupancy, limiting the maximum number of vesicles in both pools. At rest, the RRP and the TIRF-PRP are in equilibrium with on-rate constants k_{+1} and k_{+0}, and back-rates k_{-1} and k_{-0}, respectively. The probabilities of occupancy were set to 0.9 for both pools ($P_{occ,RRP}(0) = 0.9$, $P_{occ,TIRF\text{-}PRP}(0) = 0.9$); k_{+0} of 60 s^{-1} is defined by Monte Carlo simulation to fit the dwell time of "tethering–vanish" (vesicle-undocking) events in TeNT experiments (Fig. 2; $k_{-0} = k_{+0}\ (1 - P_{occ,TIRF\text{-}PRP}(0))/N_{TIRF\text{-}PRP}(0)$). Based on the assumption of an occupancy of 0.9 at rest, the apparent recruitment rate can be calculated by $60 \times 0.1 = 6\ s^{-1}$ ($= k_{+0}\ (1 - P_{occ,TIRF\text{-}PRP}(t))$). By fitting the time course of release and vanish events in control experiments, the ratio of the RRP to the PRP under resting condition ($N_{RRP}(0) = 3\ N_{TIRF\text{-}PRP}(0)$) and k_{+1} of 3 s^{-1} were obtained ($k_{-1} = k_{+1}\ N_{TIRF\text{-}PRP}(0)\ (1 - P_{occ,RRP})/N_{RRP}(0)\ (1 - P_{occ,TIRF\text{-}PRP})$). When fixing the ratio of 4, we obtained k_{+1} of 4.8 s^{-1} by fitting. The number of vesicles in the two pools at the resting state is defined by the following differential equations:

$$\frac{d}{dt}N_{RRP}(t) = k_{+1}\left(1 - P_{occ,RRP}(t)\right)N_{TIRF-PRP}(t) - k_{-1}\left(1 - P_{occ,TIRF-PRP}(t)\right)N_{RRP}(t)$$

$$\frac{d}{dt}N_{TIRF-PRP}(t) = k_{+0}\left(1 - P_{occ,TIRF-PRP}(t)\right) - k_{-0}N_{TIRF-PRP}(t)$$

$$- k_{+1}\left(1 - P_{occ,RRP}(t)\right)N_{TIRF-PRP}(t) + k_{-1}\left(1 - P_{occ,TIRF-PRP}(t)\right)N_{RRP}(t).$$

To reproduce the stimulus-induced tethering events in the model, vesicle tethering to the TIRF-PRP is forced to occur with a rate constant of 50 s^{-1}, which is the term of $k_{+0}\ (1 - P_{occ,TIRF\text{-}PRP}(t))$, at the beginning of the stimulation as we measured in control experiments. Then the rate constant decreases with time to 6 s^{-1} at ∼0.4 s. The rate constant of release (100 s^{-1}) is defined by the results of the experiments tracking the time course of release by using the different durations of the depolarizing pulse. Because capacitance increased continuously for 200 ms after a 100-ms depolarization pulse, the release rate was maintained at a constant value of 100 s^{-1} for 300 ms after the onset of the simulations. In the other simulation, we abolished the stimulus-induced tethering events without changing the other parameters (Fig. 4).

Statistical Analysis. Means and SEs were calculated in Igor or Excel (Microsoft). *P* values were determined with the Student's *t* test, Kolmogorov–Smirnov test, one-way ANOVA, and Tukey's test. Details, including sample sizes, can be found in figure legends.

Data Availability. All data are included in the manuscript and *SI Appendix*.

ACKNOWLEDGMENTS. We thank Niklas Byczkowics for developing a method for dissociating cMF terminals, and Erwin Neher, Alain Marty, and Tran Van for helpful comments on the manuscript. This work was supported by the Japan Society for the Promotion of Science (JSPS) Grants-in-Aid for Scientific Research (KAKENHI) Grants (18K06472 to T.M.; 17K19466 and 17H03548 to M.M.; and 18H02530, 19H04760, and 17H05753 to T.S.), the Uehara Memorial Foundation (to T.M.), Takeda Science Foundation (to T.M., M.M., and T.S.), the Naito Foundation (to T.M.), Brain Science Foundation (to T.M.), and JSPS Core-to-Core Program A. Advanced Research Networks (to T.S.).

1. B. Katz, *The Release of Neural Transmitter Substances*, (Liverpool University Press, Liverpool, United Kingdom, 1969).
2. J. E. Lisman, S. Raghavachari, R. W. Tsien, The sequence of events that underlie quantal transmission at central glutamatergic synapses. *Nat. Rev. Neurosci.* **8**, 597–609 (2007).
3. B. Pan, R. S. Zucker, A general model of synaptic transmission and short-term plasticity. *Neuron* **62**, 539–554 (2009).
4. E. Neher, What is rate-limiting during sustained synaptic activity: Vesicle supply or the availability of release sites. *Front. Synaptic Neurosci.* **2**, 144 (2010).
5. S. Hallermann, R. A. Silver, Sustaining rapid vesicular release at active zones: Potential roles for vesicle tethering. *Trends Neurosci.* **36**, 185–194 (2013).
6. D. Maschi, V. A. Klyachko, Spatiotemporal regulation of synaptic vesicle fusion sites in central synapses. *Neuron* **94**, 65–73.e3 (2017).
7. D. Elmqvist, D. M. J. Quastel, A quantitative study of end-plate potentials in isolated human muscle. *J. Physiol.* **178**, 505–529 (1965).
8. S. O. Rizzoli, W. J. Betz, Synaptic vesicle pools. *Nat. Rev. Neurosci.* **6**, 57–69 (2005).
9. T. Schikorski, C. F. Stevens, Morphological correlates of functionally defined synaptic vesicle populations. *Nat. Neurosci.* **4**, 391–395 (2001).
10. J. E. Richmond, R. M. Weimer, E. M. Jorgensen, An open form of syntaxin bypasses the requirement for UNC-13 in vesicle priming. *Nature* **412**, 338–341 (2001).
11. A. Betz *et al.*, Functional interaction of the active zone proteins Munc13-1 and RIM1 in synaptic vesicle priming. *Neuron* **30**, 183–196 (2001).
12. R. Jahn, D. Fasshauer, Molecular machines governing exocytosis of synaptic vesicles. *Nature* **490**, 201–207 (2012).
13. C. Imig *et al.*, The morphological and molecular nature of synaptic vesicle priming at presynaptic active zones. *Neuron* **84**, 416–431 (2014).
14. S. Chang, T. Trimbuch, C. Rosenmund, Synaptotagmin-1 drives synchronous Ca^{2+}-triggered fusion by C_2B-domain-mediated synaptic-vesicle-membrane attachment. *Nat. Neurosci.* **21**, 33–40 (2018).
15. S. M. Wojcik, N. Brose, Regulation of membrane fusion in synaptic excitation-secretion coupling: Speed and accuracy matter. *Neuron* **55**, 11–24 (2007).
16. T. C. Südhof, Neurotransmitter release: The last millisecond in the life of a synaptic vesicle. *Neuron* **80**, 675–690 (2013).
17. H. Jörntell, C. F. Ekerot, Properties of somatosensory synaptic integration in cerebellar granule cells *in vivo*. *J. Neurosci.* **26**, 11786–11797 (2006).
18. P. L. E. van Kan, A. R. Gibson, J. C. Houk, Movement-related inputs to intermediate cerebellum of the monkey. *J. Neurophysiol.* **69**, 74–94 (1993).
19. E. A. Rancz *et al.*, High-fidelity transmission of sensory information by single cerebellar mossy fibre boutons. *Nature* **450**, 1245–1248 (2007).
20. A. Ritzau-Jost *et al.*, Ultrafast action potentials mediate kilohertz signaling at a central synapse. *Neuron* **84**, 152–163 (2014).
21. C. Saviane, R. A. Silver, Fast vesicle reloading and a large pool sustain high bandwidth transmission at a central synapse. *Nature* **439**, 983–987 (2006).
22. I. Delvendahl, S. Hallermann, The cerebellar mossy fiber synapse as a model for high-frequency transmission in the mammalian CNS. *Trends Neurosci.* **39**, 722–737 (2016).
23. J. Hámori, J. Somogyi, Differentiation of cerebellar mossy fiber synapses in the rat: A quantitative electron microscope study. *J. Comp. Neurol.* **220**, 365–377 (1983).
24. P. B. Sargent, C. Saviane, T. A. Nielsen, D. A. DiGregorio, R. A. Silver, Rapid vesicular release, quantal variability, and spillover contribute to the precision and reliability of transmission at a glomerular synapse. *J. Neurosci.* **25**, 8173–8187 (2005).
25. J. J. Crowley, A. G. Carter, W. G. Regehr, Fast vesicle replenishment and rapid recovery from desensitization at a single synaptic release site. *J. Neurosci.* **27**, 5448–5460 (2007).

26. S. Hallermann *et al*., Bassoon speeds vesicle reloading at a central excitatory synapse. *Neuron* **68**, 710–723 (2010).
27. T. Miki *et al*., Actin- and myosin-dependent vesicle loading of presynaptic docking sites prior to exocytosis. *Neuron* **91**, 808–823 (2016).
28. J. S. Rothman, L. Kocsis, E. Herzog, Z. Nusser, R. A. Silver, Physical determinants of vesicle mobility and supply at a central synapse. *eLife* **5**, e15133 (2016).
29. D. Zenisek, J. A. Steyer, W. Almers, Transport, capture and exocytosis of single synaptic vesicles at active zones. *Nature* **406**, 849–854 (2000).
30. M. Midorikawa, T. Sakaba, Imaging exocytosis of single synaptic vesicles at a fast CNS presynaptic terminal. *Neuron* **88**, 492–498 (2015).
31. M. Midorikawa, T. Sakaba, Kinetics of releasable synaptic vesicles and their plastic changes at hippocampal mossy fiber synapses. *Neuron* **96**, 1033–1040.e3 (2017).
32. M. Oheim, A. Salomon, A. Weissman, M. Brunstein, U. Becherer, Calibrating evanescent-wave penetration depths for biological TIRF microscopy. *Biophys. J.* **117**, 795–809 (2019).
33. E. T. Kavalali, Synaptic vesicle reuse and its implications. *Neuroscientist* **12**, 57–66 (2006).
34. M. A. Xu-Friedman, W. G. Regehr, Ultrastructural contributions to desensitization at cerebellar mossy fiber to granule cell synapses. *J. Neurosci.* **23**, 2182–2192 (2003).
35. C. Kushmerick, R. Renden, H. von Gersdorff, Physiological temperatures reduce the rate of vesicle pool depletion and short-term depression via an acceleration of vesicle recruitment. *J. Neurosci.* **26**, 1366–1377 (2006).
36. E. Neher, T. Sakaba, Multiple roles of calcium ions in the regulation of neurotransmitter release. *Neuron* **59**, 861–872 (2008).
37. G. Schiavo *et al*., Tetanus and botulinum-B neurotoxins block neurotransmitter release by proteolytic cleavage of synaptobrevin. *Nature* **359**, 832–835 (1992).
38. T. Sakaba, Kinetics of transmitter release at the calyx of Held synapse. *Proc. Jpn. Acad., Ser. B, Phys. Biol. Sci.* **94**, 139–152 (2018).
39. C. B. Griesinger, C. D. Richards, J. F. Ashmore, Fast vesicle replenishment allows indefatigable signalling at the first auditory synapse. *Nature* **435**, 212–215 (2005).
40. R. Fernández-Busnadiego *et al*., Quantitative analysis of the native presynaptic cytomatrix by cryoelectron tomography. *J. Cell Biol.* **188**, 145–156 (2010).
41. H. de Wit *et al*., Synaptotagmin-1 docks secretory vesicles to syntaxin-1/SNAP-25 acceptor complexes. *Cell* **138**, 935–946 (2009).
42. H. Liu *et al*., Synaptotagmin 7 functions as a Ca^{2+}-sensor for synaptic vesicle replenishment. *eLife* **3**, e01524 (2014).
43. S. L. Jackman, J. Turecek, J. E. Belinsky, W. G. Regehr, The calcium sensor synaptotagmin 7 is required for synaptic facilitation. *Nature* **529**, 88–91 (2016).
44. C. Chen, R. Satterfield, S. M. Young Jr., P. Jonas, Triple function of synaptotagmin 7 ensures efficiency of high-frequency transmission at central GABAergic synapses. *Cell Rep.* **21**, 2082–2089 (2017).
45. F. Luo, T. C. Südhof, Synaptotagmin-7-mediated asynchronous release boosts high-fidelity synchronous transmission at a central synapse. *Neuron* **94**, 826–839.e3 (2017).
46. J. Turecek, W. G. Regehr, Synaptotagmin 7 mediates both facilitation and asynchronous release at granule cell synapses. *J. Neurosci.* **38**, 3240–3251 (2018).
47. A. Ritzau-Jost *et al*., Apparent calcium dependence of vesicle recruitment. *J. Physiol.* **596**, 4693–4707 (2018).
48. T. W. Rosahl *et al*., Essential functions of synapsins I and II in synaptic vesicle regulation. *Nature* **375**, 488–493 (1995).
49. L. Siksou *et al*., Three-dimensional architecture of presynaptic terminal cytomatrix. *J. Neurosci.* **27**, 6868–6877 (2007).
50. B. G. Wilhelm *et al*., Composition of isolated synaptic boutons reveals the amounts of vesicle trafficking proteins. *Science* **344**, 1023–1028 (2014).
51. G. Kusick *et al*., Synaptic vesicles undock and then transiently dock after an action potential. bioRxiv:10.1101/509216 (31 December 2018).
52. L. Maus *et al*., Ultrastructural correlates of presynaptic functional heterogeneity in hippocampal synapses. *Cell Rep.* **30**, 3632–3643.e8 (2020).
53. H. von Gersdorff, G. Matthews, Depletion and replenishment of vesicle pools at a ribbon-type synaptic terminal. *J. Neurosci.* **17**, 1919–1927 (1997).
54. S. Iwasaki, T. Takahashi, Developmental regulation of transmitter release at the calyx of Held in rat auditory brainstem. *J. Physiol.* **534**, 861–871 (2001).
55. E. Neher, N. Brose, Dynamically primed synaptic vesicle states: Key to understand synaptic short-term plasticity. *Neuron* **100**, 1283–1291 (2018).
56. W. J. Jockusch *et al*., CAPS-1 and CAPS-2 are essential synaptic vesicle priming proteins. *Cell* **131**, 796–808 (2007).
57. Y. Lai *et al*., Molecular mechanisms of synaptic vesicle priming by Munc13 and Munc18. *Neuron* **95**, 591–607.e10 (2017).
58. E. He *et al*., Munc13-1 and Munc18-1 together prevent NSF-dependent de-priming of synaptic vesicles. *Nat. Commun.* **8**, 15915 (2017).
59. T. Miki, Y. Nakamura, G. Malagon, E. Neher, A. Marty, Two-component latency distributions indicate two-step vesicular release at simple glutamatergic synapses. *Nat. Commun.* **9**, 3943 (2018).
60. N. Hosoi, M. Holt, T. Sakaba, Calcium dependence of exo- and endocytotic coupling at a glutamatergic synapse. *Neuron* **63**, 216–229 (2009).
61. R. A. Silver, J. Lubke, B. Sakmann, D. Feldmeyer, High-probability uniquantal transmission at excitatory synapses in barrel cortex. *Science* **302**, 1981–1984 (2003).
62. K. D. Gillis, Admittance-based measurement of membrane capacitance using the EPC-9 patch-clamp amplifier. *Pflugers Arch.* **439**, 655–664 (2000).